Dissipation of Turbulent Kinetic Energy Inferred from Seagliders: An Application to the Eastern Nordic Seas Overflows

NICHOLAS BEAIRD

School of Oceanography, University of Washington, Seattle, Washington

ILKER FER

Geophysical Institute, University of Bergen, Bergen, Norway

PETER RHINES AND CHARLES ERIKSEN

School of Oceanography, University of Washington, Seattle, Washington

(Manuscript received 31 May 2012, in final form 16 August 2012)

ABSTRACT

Turbulent mixing is an important process controlling the descent rate, water mass modification, and volume transport augmentation due to entrainment in the dense overflows across the Greenland–Scotland Ridge. These overflows, along with entrained Atlantic waters, form a major portion of the North Atlantic Deep Water, which pervades the abyssal ocean. Three years of Seaglider observations of the overflows across the eastern Greenland–Scotland Ridge are leveraged to map the distribution of dissipation of turbulent kinetic energy on the Iceland–Faroe Ridge. A method has been applied using the finescale vertical velocity and density measurements from the glider to infer dissipation. The method, termed the large-eddy method (LEM), is compared with a microstructure survey of the Faroe Bank Channel (FBC). The LEM reproduces the patterns of dissipation observed in the microstructure survey, which vary over several orders of magnitude. Agreement between the inferred LEM and more direct microstructure measurements is within a factor of 2. Application to the 9432 dives that encountered overflow waters on the Iceland–Faroe Ridge reveals three regions of enhanced dissipation: one downstream of the primary FBC sill, another downstream of the secondary FBC sill, and a final region in a narrow jet of overflow along the Iceland shelf break.

1. Introduction

The Faroe Bank Channel (FBC) and its smaller neighboring overflow across the Iceland–Faroe Ridge (IFR) account for one-third of total Nordic Seas outflow into the North Atlantic (Hansen and Østerhus 2000). Considerable effort has been focused on the region in general and on the FBC in particular. Along with entrained Atlantic waters, which double the initial overflow volume transport, these overflows make up a large part of the North Atlantic Deep Water (NADW). NADW has global extent in the deep ocean and its circulation forms the lower limb of the Atlantic meridional overturning circulation. The location and intensity of turbulent mixing and entrainment in these overflows has an important impact on ventilation of the deep ocean and the oceanic meridional heat transport. Entrainment of overlaying waters is particularly interesting in this region where wintertime mixed layers can sometimes reach the depth of the overflow plume interface.

A comprehensive review of North Atlantic–Nordic Seas exchanges is given by Hansen and Østerhus (2000) and of the FBC overflow by Hansen and Østerhus (2007). At the sill thresholds, approximately 3 Sv (Sv $\equiv$ 10^6 m^3 s^{-1}) of Nordic origin waters form energetic bottom-intensified gravity currents flowing into the Iceland Basin. Of the total 3 Sv, 1.9 Sv exits through the FBC, and the remainder crosses the IFR. The Faroe Bank Channel overflow is swift [O(1 m s^{-1})] and unidirectional, with a bottom mixed layer of cold (~0°C) water capped by a thick [O(100 m)] interfacial layer below the ambient Atlantic waters. Dissipation levels

Corresponding author address: Nicholas Beaird, University of Washington, 1492 NE Boat St., Seattle, WA 98195.
E-mail: nlbeaird@uw.edu

DOI: 10.1175/JPO-D-12-094.1

as high as 10^{-5} W kg^{-1} illustrate the energetic turbulence at work in the overflow (Fer et al. 2010). The FBC overflow exhibits considerable mesoscale variability, which plays a role in the mixing and descent of the plume (Darelius et al. 2011; Seim and Fer 2011). After exiting the FBC, the overflow plume makes an inertial turn to the right and flows along isobaths on the Atlantic flank of the IFR, driven by a balance of pressure gradient, Coriolis, and frictional forces. As it flows downstream, the plume descends slightly due to the frictional relaxation of the geostrophic constraint. The FBC plume is joined along this path by overflow from the IFR, which is more spatially intermittent but has very similar source waters.

By the time these waters have traveled downstream to form Northeast Atlantic Deep Water (NEADW) their volume flux will have doubled to 6 Sv and their temperature and salinity properties will be significantly diluted by entrainment of overlying Atlantic waters. These overflows occur in physically small regions (the FBC sill is ~10 km wide), exhibit complex submesoscale flow features, and depend intimately on very small scale mixing processes. Despite the small scales of the overflows, their influence is felt on basin, planetary, and climatic scales. It is critical, but notoriously difficult, to represent overflows in numerical models (Legg et al. 2009). The intensity of mixing and entrainment in the overflow plumes affects their eventual volume flux, descent rate, end-member properties and detrainment depth. In addition to the obvious effect on plume properties, recent studies of the Mediterranean Outflow also suggest that the upper ocean responds directly to the potential vorticity forcing from the descent and entrainment of overflows (Kida et al. 2008).

Several indirect mixing estimates (mainly based on heat budgets) have been made in the FBC (Saunders 1990; Duncan et al. 2003; Mauritzen et al. 2005), while more recently the first direct microstructure turbulence measurements have been made by Fer et al. (2010), all of which indicate intense mixing in the FBC plume downstream of the sill. These studies are important to facilitate understanding of mixing in the overflows; however, in each case the shipboard surveys only lasted a short time. The well-documented variability of the FBC overflow (Geyer et al. 2006; Darelius et al. 2011) and the myriad locations of IFR overflow suggest that more complete time series and higher spatial resolution of mixing estimates are desirable.

In this paper a three year dataset of Seaglider observations in the FBC and on the IFR is used to obtain a more complete spatial picture of the mixing and entrainment in these overflows. These data extend 300 km farther downstream than the majority of the FBC overflow studies mentioned above and offer the first look at turbulence in the IFR overflows. The analysis presented here hinges on the development of a method to obtain estimates of dissipation of turbulent kinetic energy (ε) from the Seaglider. The method is developed and then validated by comparison between a Seaglider deployment and a contemporaneous microstructure survey (Fer et al. 2010).

2. Measurements

The data presented in this study come from two sources: one shipboard and one Seaglider survey. Ancillary data include approximately 2-month-long measurements from a moored instrument located at the center of the shipboard and Seaglider surveys. The glider data were collected over three years between November 2006 and November 2009. Deployments were made every three months, with 23 successful missions producing roughly 17 400 profiles of temperature, salinity, dissolved oxygen, fluorescence, optical backscatter, and vertical velocity in the Iceland–Faroes region.

The Seaglider is a small, autonomous, buoyancy-driven vehicle that profiles to a maximum depth of 1000 m in a sawtooth pattern (Eriksen et al. 2001). The gliders deployed in this survey were equipped with unpumped custom Sea-Bird Electronics conductivity (SBE 4) and temperature (SBE 3) sensors, a Wetlabs BB2FVMG optical puck with florescence and two wavelengths of backscatter, and a Sea-Bird Electronics oxygen sensor (SBE 43). During the Faroes mission, the gliders sampled water column properties at 20-s intervals. With typical vehicle descent/ascent rates of 6–10 cm s^{-1}, the vertical resolution of the profiles was approximately 1.2–2 m. The vertical to horizontal glide ratio of 1:3 gives horizontal resolution of 3.6–6 m between consecutive samples, while dive and climb profile separations vary with depth owing to the slant-vertical path of the instrument. Adjacent glider surfacings are typically 3 to 6 km apart. An acoustic altimeter mounted forward on the Seaglider is used to detect and avoid the seafloor. To fully sample the overflow plume, these gliders were programed to begin their dive-to-climb transition 10 m above the acoustically ranged bottom.

The distribution of the Seaglider data in the FBC and downstream on the IFR is shown in Fig. 1. Each point in the figure represents one dive/climb profile pair and color indicates the bottom temperature, or the temperature at the deepest observation made by the instrument. Typically Seagliders were deployed in the FBC where they remained for several days as the pilot trimmed flight control parameters. Trimmed vehicles were subsequently flown northwestward along isobaths of the

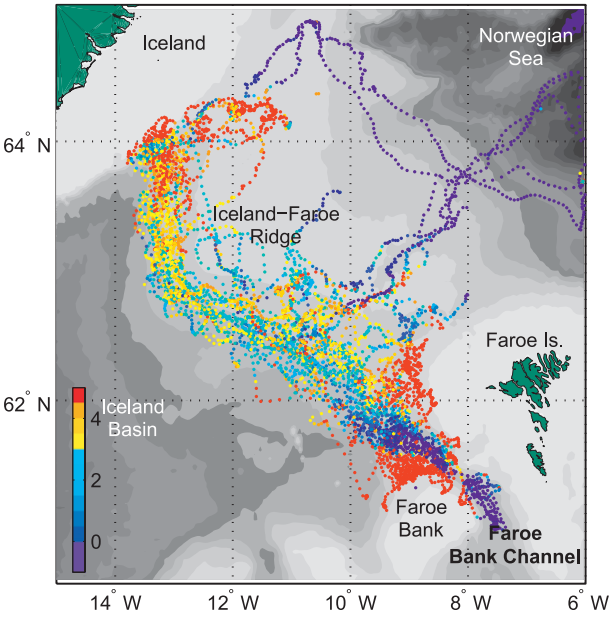

FIG. 1. Location of all Seaglider dives on the Iceland–Faroe Ridge from November 2006 through November 2009. Each dot indicates the location of one dive/climb pair. Color is proportional to the bottom temperature (°C) with color scale indicated at bottom left.

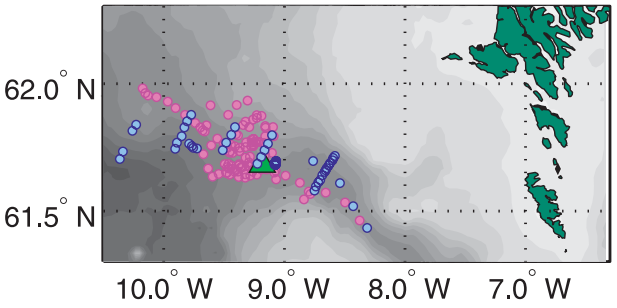

FIG. 2. Location of 57 VMP casts from the 2008 cruise (blue circles), the sg005 June 2008 dives in the FBC (magenta circles), and mooring B2 (green triangle).

IFR. After reaching the Iceland shelf break the gliders were piloted back to the FBC or, on occasion, across the IFR into the Norwegian Basin.

The shipboard survey was made from the R.V. *Håkon Mosby* during the period 29 May–8 June 2008 (Fer et al. 2010). During the cruise, 90 profiles were collected using a vertical microstructure profiler (VMP2000, Rockland Scientific Instruments, VMP hereafter). The VMP had a depth rating of 2000 m and was equipped with pumped-SBE conductivity–temperature–depth (CTD) sensors, a pair of airfoil shear probes used for measuring the dissipation rate of turbulent kinetic energy (ε), and fast response temperature and conductivity sensors. The turbulence and slow sensors sampled at 512 and 64 Hz, respectively, at a nominal profiling speed of 0.6 m s^{-1}. Stations were taken on six cross sections along the path of the overflow plume starting from the sill crest to about 120 km downstream of the sill, a downstream section, as well as two repeat stations of approximately 12-h duration (Fig. 2). The downcast of the VMP typically reached 10–50-m height above bottom (HAB). The profiles of ε were obtained from the shear probes of the VMP as 1-m vertical averages by integrating the vertical wavenumber spectrum of shear and assuming isotropy. The lowest detection level (noise level) in ε measurements based on shear probe data in the quiescent portions of the water column was 10^{-10} W kg^{-1}. Details on the sampling and data processing can be found in Fer et al. (2010) and Seim and Fer (2011).

Additionally, we make use of vertical velocity and temperature measurements acquired by temperature loggers and a downward looking acoustic Doppler current profiler (ADCP, RDI 300-kHz Workhorse Sentinel), moored at 61°41′N, 9°11′W at the 804-m isobath, between 14 May and 18 July 2008. The mooring is located about 60 km downstream of the FBC sill, referred to as B2 in Darelius et al. (2011) and CM in Seim and Fer (2011). We refer to the mooring as B2, consistent with Darelius et al. (2011). The ADCP installed in a spherical buoy at 200 m HAB ensemble averaged 50 profiles every 5 min with 2-m vertical depth bins, returning high quality data with negligible tilt from vertical (1.6 ± 0.7° roll and −1.4 ± 0.7° pitch). Temperature time series were recorded by a number of temperature (SBE39 and RBR TR-1050) and CTD (SBE37 MicroCAT) sensors mounted on the mooring at 20, 101, 148, 140–200 (10-m intervals), 201 and 210 m HAB. Vertical displacements of the instruments due to horizontal currents were calculated following Dewey (1999), and temperature records were linearly interpolated onto a vertical grid using the inferred instrument depths (Darelius et al. 2011). The time series of the HAB of the 3°C isotherm is used to highlight the low-frequency variability associated with the FBC overflow. A more complete description of the moored instruments, data processing, and discussion on mesoscale variability and plume dynamics can be found in Darelius et al. (2011) and Seim and Fer (2011).

A comparison will be made between the dissipation measurements from the VMP and the estimates from a concurrent Seaglider deployment. Seagliders are designated by the letters "sg" followed by a serial number. Around the time of the VMP survey in June 2008, Seaglider 5 (sg005) was deployed in the Faroe Bank Channel. The data from sg005 will be compared with the VMP survey to determine calibration coefficients for the Seaglider ε estimate.

3. Methods

a. Vertical velocities from Seaglider

The Seaglider can furnish an estimate of vertical water velocity w by taking advantage of an accurate vehicle flight model and its on board pressure sensor. The validity of the flight model assumptions is critical, but in principal the w estimate is straightforward: the vehicle vertical speed through a quiescent ocean, w_{model}, is calculated by a flight model using the measured pitch and buoyancy, while the absolute vertical speed is calculated from the time rate of change of pressure onboard the glider, w_{meas}. Removing the relative vehicle speed from the absolute gives the ambient water vertical velocity: $w = w_{\text{meas}} - w_{\text{model}}$. Detailed descriptions of the flight model and the process of determining w may be found in Frajka-Williams et al. (2011) and Eriksen et al. (2001). We will reproduce the basics of the calculation here.

Assuming steady flight, the force balance on the Seaglider is between the lift (L) from the wings, the drag (D) on the body, and the glider's excess buoyancy (B):

$$L = \mathcal{P}h^2 a\alpha = -B\cos\theta, \tag{1}$$

$$D = \mathcal{P}h^2(bq^{-(1/4)} + c\alpha^2) = B\sin\theta, \tag{2}$$

$$B = g[-M + \rho V(t, p, T)], \tag{3}$$

where h is the hull length, α the attack angle, θ the glide-slope angle; a, b, c are the lift, drag, and induced drag coefficients respectively; g is gravitational acceleration, M the vehicle mass, $V(t, p, T)$ the total vehicle volume as a function of time (t, a result of controlled pumps/bleeds of hydraulic oil between reservoirs interior and exterior to the pressure hull), pressure (p), and temperature (T), and $\mathcal{P}$ is the dynamic pressure. The glide-slope angle (θ) is the angle between the horizontal and the trajectory of flight, while the attack angle (α) is the angle between the chord line of the glider wings and the direction of the incident fluid. The distinction is critical because the glider can only measure its pitch angle (ϕ) from the inclinometer, but lift and drag are functions of the attack angle, while the glide-slope angle describes the ratio of vertical to horizontal motion through the water. The glide-slope and attack angles are related to the measured pitch angle by $\phi = \alpha + \theta$. The dynamic pressure term contains the velocity information, $\mathcal{P} = \rho(U^2 + W^2)/2$, where U and W are the horizontal and vertical glider speeds and ρ is the water density. The functional forms of lift and drag in Eqs. (1) and (2) are based on hydrodynamic testing of the vehicle shape (Hubbard 1980). The flight model is sensitive to the values of the flight parameters a, b, and c and the total vehicle volume $V(t, p, T)$, all of which must be independently determined for each Seaglider. The flight equations (1) and (2) are solved iteratively for $\mathcal{P}$ and α. Finally, the modeled vertical vehicle speed is calculated from the dynamic pressure and glide angle as

$$w_{\text{stdy}} = \sqrt{\frac{2\mathcal{P}}{\rho}}\sin\theta. \tag{4}$$

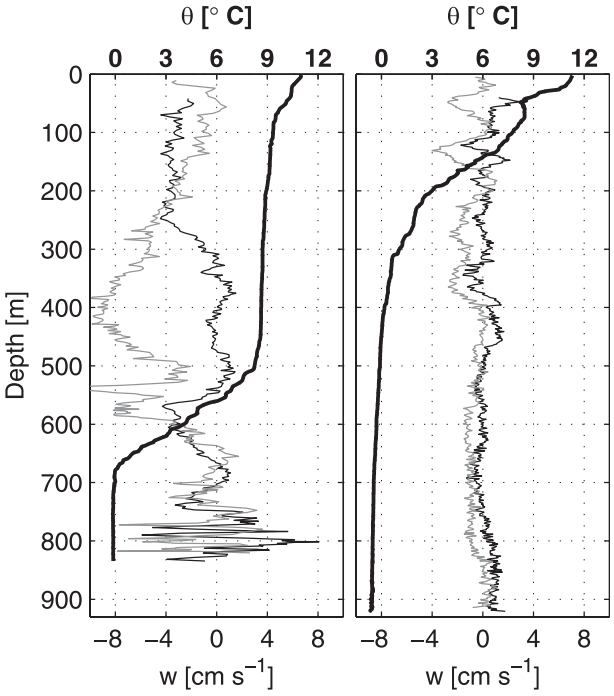

FIG. 3. Velocity profiles from the dives (black) and climbs (gray) as well as potential temperature (thick black, refer to top axis) from two Seaglider dives: (left) a dive in the FBC into the overflow plume and (right) a dive in a calm, deep, region north of the IFR in the open Norwegian Sea.

Figure 3 provides examples of the resulting vertical velocity profiles from two Seaglider dives. The profile from a dive in the FBC that passes through the energetic overflow plume (Fig. 3, left) is significantly more energetic than the profile in the deep quiescent region north of the IFR in the Norwegian Sea (Fig. 3, right). Additionally, it is relevant to the dissipation estimate method outlined below to note that the vertical velocity variance at high vertical wavenumbers increases in the FBC overflow plume (Fig. 3, left, depth $\gtrsim$ 700 m).

Recent analysis of Seaglider deployments in the Labrador Sea shows sensible w fields in stratified and deeply convecting regions. The Labrador Sea Seaglider w observations of Frajka-Williams et al. (2011) indicate

that the root-mean-square w roughly scales with the amplitude of the surface forcing, for low stratification WKB scaling holds, and the vertical wavenumber and amplitude of w profiles increase within the surface mixed layers associated with deep convection. A similar determination of w has been carried out on Slocum gliders in the Mediterranean Sea (Merckelbach et al. 2010), again illustrating the possibility of using gliders to observe oceanic vertical velocities.

Spectra were used to assess noise in the Seaglider vertical velocity measurement. Profiles were taken from a constant stratification portion of the water column (400–900 m) in the open, quiescent, Norwegian Basin. The spectra were integrated from where the slope flattened (1/240 Hz) to the Nyquist frequency (1/40 Hz) to find noise variance. Six different gliders in the region suggest similar Seaglider w error estimates of ± 0.2 cm s^{-1}. It should be noted that this value is considered the precision of the w measurement, not the accuracy. It is possible that a full depth offset, or low-frequency systematic error exists due to improperly known values of the Seaglider vehicle volume or compressibility. However, as will be mentioned below, a high-pass filter is used in this analysis to look at velocity fluctuations, making offsets and low frequency errors irrelevant. Therefore we adopt an error estimate of 0.2 cm s^{-1}, consistent with the application outlined below.

b. Large-eddy method

The method of estimating dissipation employed in this analysis is based on a simple scaling of the turbulent kinetic energy (TKE) equation (Taylor 1935). We refer to this scaling as the ''large-eddy method'' (LEM). The method relies on the hypothesis (Kolmogoroff 1941) that a steady turbulent energy cascade exists, which allows measurements of the relatively large energy-containing scales to be used to infer the energy loss at viscous scales (Moum 1996). Energy is introduced to the turbulent flow by instabilities in the large-scale mean. In a steady state, this energy must be passed to smaller and smaller scales until it can be dissipated by viscosity. Described by the Kolmogoroff scale, $\eta = (\nu^3/\varepsilon)^{1/4}$, the dissipation scale for ocean turbulence can be on the order of millimeters. This level of spatial resolution is well beyond the sampling capacity of the standard Seaglider. Assuming no leakage of energy (by, for example, nondissipative linear internal waves), the cascade of TKE may be described by the energy of the largest eddies in the turbulent flow and their overturning time scale (Tennekes and Lumley 1972). We let q' be a velocity scale of the largest eddies, and l be their length scale. The eddy time scale may be written as $\tau \sim l/q'$ and dissipation ε scales as

$$\varepsilon \sim \frac{(q')^2}{\tau} \sim \frac{(q')^3}{l}. \tag{5}$$

A physical interpretation of Eq. (5) is that the kinetic energy $(q')^2$ of a turbulent eddy is dissipated in the time it takes to overturn once $\tau \sim l/q'$.

This scaling has been investigated by many authors including Moum (1996), Peters et al. (1995), and Gargett (1999). These authors find that the scaling holds in a variety of oceanic regimes, including regions of low average dissipation containing sporadic energetic events (Peters et al. 1995). For stratified flow, a modification may be obtained by using the Ozmidov length $L_{Oz} = \varepsilon^{1/2}N^{-3/2}$ for l in Eq. (5). The Ozmidov length is a measure of the maximum vertical overturn displacement that may occur for a given turbulent energy level and stratification (Thorpe 2005). Rearranging Eq. (5), using $l = L_{Oz}$ and introducing a proportionality constant c_ε, leads to an expression for the estimate (e) of dissipation of TKE that is explicitly independent of l:

$$e = c_\varepsilon N(q')^2. \tag{6}$$

Use of the Ozmidov scaling in Eq. (6) is equivalent to assuming that the overturning time scale of the largest eddies is $1/N$. D'Asaro and Lien (2000a) investigate the scaling in Eq. (6) in their discussion of the wave–turbulence transition, finding that it should hold in sufficiently high energy environments. The high energy regime where Eq. (6) holds is defined in D'Asaro and Lien (2000b) as the ''stratified turbulence'' regime where the internal wave bandwidth of the vertical wavenumber shear spectra becomes small. The shear spectra in Fig. 14 of Seim et al. (2010) indicate the FBC is energetic enough to be considered part of the stratified turbulence regime.

Equation (6) is, of course, still implicitly dependent on a length scale, the length scale over which the velocity fluctuations are calculated. The appearance of the buoyancy frequency N in Eq. (6) may also prove problematic for well-mixed layers; however, we still find it advantageous to have an ''l-less'' estimate of ε. Following Gargett (1999) we will use the vertical velocity w to define the velocity scale q'. D'Asaro and Lien (2000a) note that, for stratified flows with a large internal wave component, kinetic energy is anisotropic and concentrated in the horizontal motions of the waves. Vertical kinetic energy, however, is nearly equipartitioned between waves and turbulence, making vertical kinetic

energy a more appropriate choice to study turbulence (D'Asaro and Lien 2000a). Unlike the ADCP measurements in Gargett (1999), who must use the velocity profile to define both q' and l in Eq. (5), we have parallel density measurements that we use to define the buoyancy frequency used in Eq. (6). We determine c_ε by a comparison of bulk dissipation properties of the FBC as observed from sg005 and the 2008 microstructure survey.

c. Choosing the scales

To proceed with the estimate of dissipation the velocity and length scales must be determined. We are interested in the kinetic energy and length scales of the largest turbulent motions in the flow field that lead to dissipation. Therefore, the influence of nondissipative motions such as linear internal waves must be suppressed. A strict scale separation between the internal wave regime and the turbulent regime does not exist in the ocean, and separating turbulent and internal wave motions has been a long standing problem. However, low vertical wavenumber motions that are clearly related to internal waves or tidal frequency motions may be removed from the Seaglider w record.

In the first step toward obtaining the velocity scale q', a high-pass filter is run over the full $w(z)$ profile to obtain a profile of high frequency velocity fluctuations $w_{\rm hp}(z)$. The filter removes energy associated with low wavenumber motions that are clearly not related to turbulent overturns and has the added benefit of reducing errors associated with any improperly determined flight parameters. As Frajka-Williams et al. (2011) point out, adjustments to the flight model parameters tend to influence low frequency characteristics of the $w(z)$ profile, for example the full depth offsets or large scale divergence. Using $w_{\rm hp}(z)$ removes these low frequency error signals. As noted previously, it is not guaranteed that the filter removes all internal wave motions. We will rely on the agreement between the LEM and VMP dissipation estimates to determine whether nondissipative motions have been satisfactorily removed.

A fourth-order Butterworth high-pass filter with a lower cutoff wavelength λ_c of 30 m is used. For cutoff lengths shorter than 100 m, the method does not appear to be sensitive to the exact choice of λ_c. A larger λ_c produces higher values of the dissipation estimate profile, which in turn requires a smaller value of c_ε to match the VMP data, but no change in profile shape is evident until λ_c exceeds about 100 m. It is possible that in the FBC the energetic internal wave field leads to this insensitivity. The internal wave field is greatly enhanced relative to the Garrett–Munk spectrum (Fer et al. 2010). The internal waves may be highly nonlinear in the FBC, leading to significant breaking and dissipation. Thus, if much of the internal wave energy is dissipated locally, a larger λ_c that includes some internal wave energy does not reduce the agreement of the LEM with the VMP dissipation estimates. With this possibility in mind, the smallest λ_c possible has been chosen to allow application of the LEM to regimes other than the FBC. A value of $\lambda_c = 30$ m corresponds to about 300 s of glider flight or about 15 sample intervals. Finally, the velocity scale q' is calculated as the rms value of the $w_{\rm hp}(z)$ profile over a moving 10-m window. The window ensures that q' is a representative velocity scale over several eddy length scales, which we take to be on the order of the Ozmidov scale. For comparison, the implied Ozmidov scale (calculated from the Seaglider LEM measurements) in the FBC is approximately lognormally distributed and has a maximum likelihood estimate (standard deviation) of 0.77 (2.4) m. The corresponding values from the VMP survey are 0.51 (3.13) m.

Several choices of length scale have been explored. The first, Thorpe displacements (d'), are calculated as the vertical distance between the depths of a given isopycnal in an observed profile and in the profile resorted into its statically stable equivalent. The Thorpe scale $L_{\rm Th}$ is then obtained by taking the root-mean-square of d' over the vertical extent of an individual overturn event. The Thorpe scale has the advantage of being a direct measurement of overturning scales and of being unaffected by internal wave motions. However, the Seaglider vertical sampling resolution of 1.2–2 m is coarse relative to typical $L_{\rm Th}$ values, particularly in regions of strong stratification. Additionally, the slant profiling pattern of the Seaglider could produce spurious $L_{\rm Th}$ in strong horizontal gradient regions near Kelvin–Helmholtz instabilities or steep internal waves (Smyth and Thorpe 2012). Furthermore, it is possible to infer dissipation directly from Thorpe displacements, in some cases, using the relation $\varepsilon_{\rm Th} = 0.64 L_{\rm Th}^2 N^3$ (Dillon 1982) and therefore adding a dependence on w may introduce undue complication. The full analysis described below was also carried out using Thorpe displacements in Eq. (5), and the results were not qualitatively different from those presented. However, as mentioned above, the length scale chosen for the LEM presented here is $L_{\rm Oz}$.

The Ozmidov length scale was chosen for several reasons. First, the definition of $L_{\rm Oz}$ as the largest scale at which overturns may occur for a particular turbulent energy level and stratification is consistent with the physical interpretation of the LEM. Additionally, the revised formulation [Eq. (6)] leads to a continuous dissipation profile, unlike the Thorpe displacements which give undefined values of e where $L_{\rm Th} = 0$ or is below the vertical resolution of the observations, which is the case for much of the record. Finally, previous studies have shown the scaling in Eq. (5)

with $l = L_{Oz}$ to have better agreement with dissipation-scale estimates than Eq. (5) with $l = L_{Th}$ (Moum 1996). Equation (6) is employed throughout the following analysis.

4. Method validation

VMP and Seaglider comparison survey

A procedure for calculating $q'(z)$, and hence e, has been outlined above. To complete the estimate of dissipation, the proportionality constant c_ε was determined by calibration with the 2008 VMP survey. Of the 90 VMP casts collected, 57 are close to the Seaglider survey region and have been used for the comparison. These are shown in blue in Fig. 2. From the full three month deployment, 108 dives of sg005 were selected for comparison and are plotted in magenta in Fig. 2. The Seaglider was launched 21 h after the VMP survey was completed, making a direct calibration of the large-eddy method impossible. Instead, survey-averaged profiles and probability distribution functions of dissipation were used. When calculating survey-averaged profiles from both the Seaglider and the VMP, only casts that encounter the overflow plume have been considered. It will be shown below that both VMP and Seaglider surveys adequately sampled the mesoscale variability of the overflow.

As a consistency check on the Seaglider vertical velocities in the FBC, the distribution of w observations from sg005 was compared with the downward looking ADCP on mooring B2 (Fig. 4). ADCP vertical velocity was collected from each of the useable 2-m vertical depth bins, which are 6 to 66 m below the instrument—nominally between 610 and 676 m—but, due to current-induced knockdown, the ensonified region varies between 594 m and 690 m. Typically the ADCP measured the interfacial layer between the plume and the ambient Atlantic above. The Seaglider vertical velocities were taken from 42 dives located within 10 km of the mooring. The distribution of Seaglider observed w from depths between 600 and 700 m is plotted in the bottom panel of Fig. 4. The distributions of ADCP and Seaglider derived w overlap and have similar means and standard deviations: mean (std dev.) for the glider is -0.29 (2.9) cm s^{-1} and for the ADCP is -0.73 (2.5) cm s^{-1}. A quantile–quantile plot in the upper panel of Fig. 4 plots the empirical distribution of the ADCP velocities against that of the Seaglider. The linear relationship indicates the similarity of the two distributions and increases our confidence in the Seaglider w measurement.

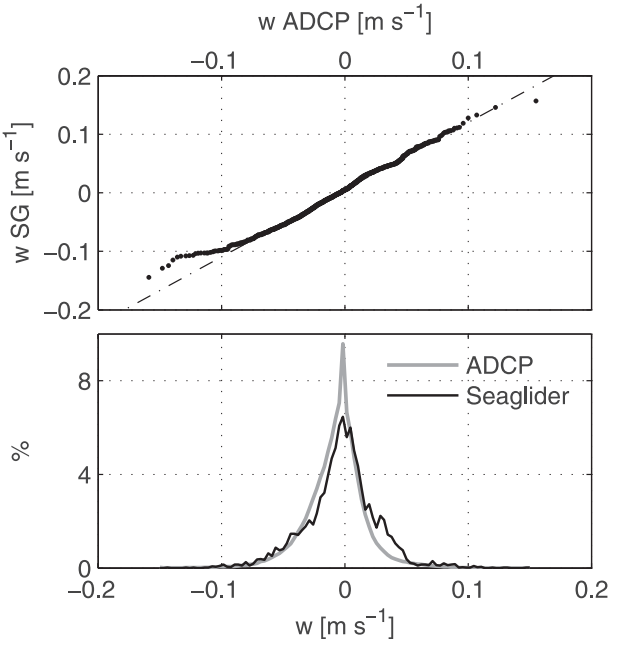

FIG. 4. (top) The empirical distributions of vertical velocity w from the ADCP (x axis) vs that of sg005 (y axis) in a quantile–quantile plot. (bottom) Histograms of vertical velocity from the ADCP on mooring B2 (gray) and from 42 dives made by sg005 (black) within 10 km of B2. Velocities are measured between 600 and 700 m by the glider and between 594 and 690 m by the ADCP.

1) SURVEY-AVERAGED PROFILES

The height-above-bottom of the 3°C isotherm, a good indication of the maximum stratification in the interface between the overflow plume and the overlaying Atlantic water, is plotted against yearday of 2008 in Fig. 5. The strong mesoscale variability of the overflow with a period of about 3.5 days is readily apparent. This overflow variability has been documented by other authors and has significant dynamical consequences for the plume (Geyer et al. 2006; Darelius et al. 2011). The oscillation must be taken into consideration when comparing the Seaglider and VMP surveys. Thick and thin vertical lines at the bottom of Fig. 5 indicate the times of VMP casts and Seaglider dives. The gap around yearday 157 shows the 21-h delay between the end of the VMP cruise and the beginning of the sg005 mission. Evidently both VMP and sg005 sample all phases of the mesoscale variability, as can be seen from the temporal coverage of the two surveys. Average profiles will be unbiased with respect to the phasing of the oscillation. We may reasonably expect the average profiles to be comparable between the two instruments and representative of the mean conditions of the overflow plume.

In light of the presence of the mesoscale oscillation, the survey-averaged profiles of the VMP and sg005 presented in Fig. 6 have been calculated with three different vertical coordinates: the shallowest 200 m was computed with respect to the surface; the bulk of the

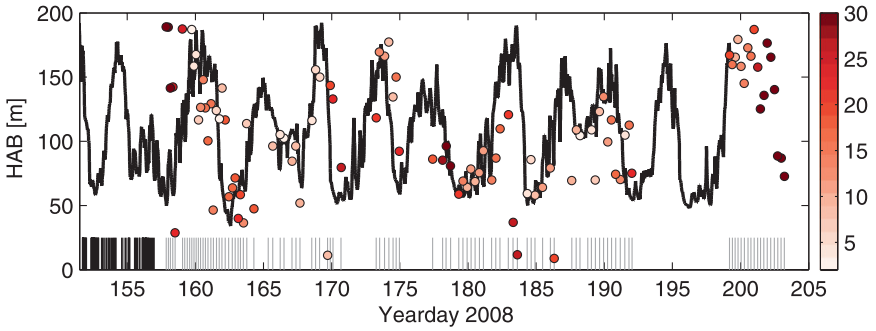

FIG. 5. Time series of the height-above-bottom (HAB) of the 3°C isotherm from the B2 mooring (black). Short vertical lines indicate the times when the VMP casts (black) or sg005 dives (gray) took place. Colored dots are plotted at the HAB of the 3°C isotherm as seen by the Seaglider, and their color indicates the distance (km) between sg005 and mooring B2.

water column was calculated with respect to vertical distance from the 3°C isotherm; and the bottom 150 m were averaged with respect to height above the bottom. A linear least squares fit between the Seaglider LEM and the VMP survey-averaged profiles produced a proportionality constant $c_\varepsilon = 0.37$, resulting in the survey-averaged profile in Fig. 6c. This value is broadly consistent with previous studies using Eq. (6), for example $c_\varepsilon = 0.3 - 0.6$ in D'Asaro and Lien (2000b) and $c_\varepsilon = 0.73 \pm 0.06$ in Moum (1996). The noise level, that is, the lowest detection limit, of the LEM was found by substituting the velocity noise $w = 0.002$ m s^{-1} (section 3a) into Eq. (6), giving

$$e_{\text{noise}} = (1.4 \times 10^{-6})N. \quad (7)$$

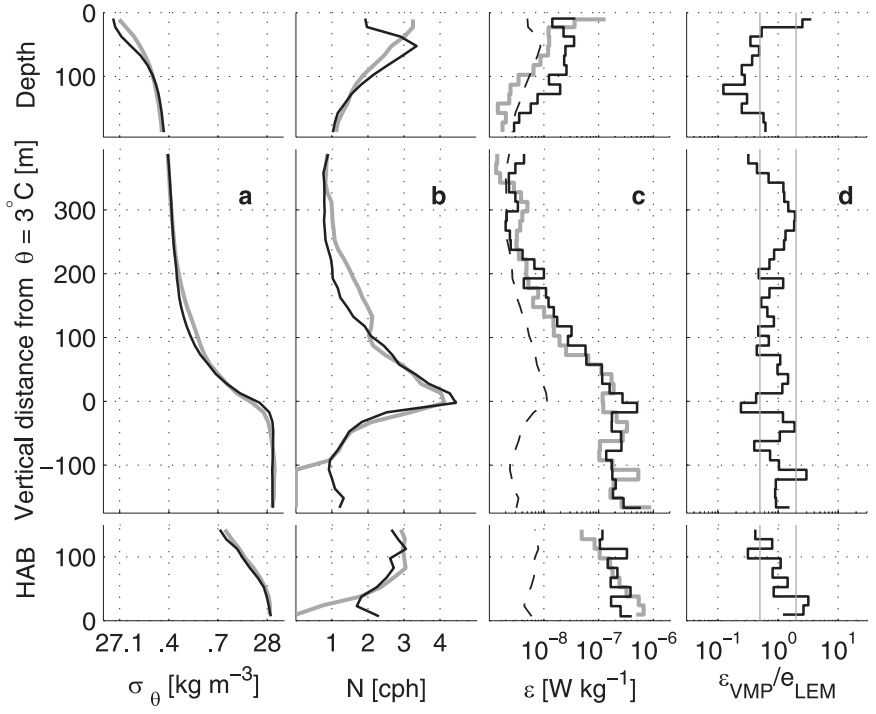

FIG. 6. Survey-averaged profiles of (a) potential density anomaly σ_θ, (b) buoyancy frequency N, (c) dissipation of TKE ε, and (d) ratio of VMP to sg005 dissipation estimates. VMP profiles are plotted in gray; Seaglider (sg005) profiles in black. Profiles are averaged with respect to (top) depth, (middle) distance from the 3°C isotherm, and (bottom) height above bottom in 15-m bins. Average noise level (i.e., lowest detection level) for the LEM [Eq. (7)] is plotted as a dashed black line in (c). Light gray lines in (d) show factor of 2 bounds on the estimate ratio.

For typical FBC buoyancy frequencies ranging between 1 and 4 cph, Eq. (7) gives e_{noise} between 2.5×10^{-9} and 1×10^{-8} W kg^{-1}. The survey-averaged profile of e_{noise} is plotted as a dashed line in Fig. 6c.

Figure 6a shows the typical vertical density structure of the FBC region. Near the surface, a seasonal pycnocline overlies a thick, modestly-stratified, layer of Atlantic water ($27.4 \lesssim \sigma_\theta \lesssim 27.6$ kg m^{-3}). The Atlantic layer then lies above a high stratification interface ($27.6 \lesssim \sigma_\theta \lesssim 27.9$ kg m^{-3}) capping the relatively well mixed overflow plume ($\sigma_\theta \gtrsim 27.9$ kg m^{-3}). Dissipation of TKE (Fig. 6c) varies over 2.5 orders of magnitude throughout the water column. Dissipation is elevated near the surface, falls to a minimum in the Atlantic water above the interface, and gradually increases with depth until the overflow plume layer is reached, remaining high to the bottom. The Seaglider dissipation estimate falls to near its noise level in the Atlantic waters around 250 m above the 3° isotherm. The Seaglider LEM and the VMP dissipation estimates covary over the full water column (Fig. 6c). Because of the large number of observations that go into the average profiles, 95% confidence intervals are very tight. A more reasonable indication of the agreement between the Seaglider LEM and the VMP is found by looking at the ratio of the survey-averaged profiles (Fig. 6d). The vertical mean (std dev) of $\varepsilon_{\text{VMP}}/e_{\text{LEM}}$ referenced to the 3° isotherm (Fig. 6d, center row) is 1.01 (0.53). Faint gray lines in Fig. 6d show that the Seaglider LEM agrees with the VMP to within a factor of 2. A two sample Kolmogoroff–Smirnoff test of the survey-averaged profiles in Fig. 6c shows no significant differences in the distributions of the Seaglider LEM and the VMP dissipation.

In Fig. 7 the same ratio of survey-averaged dissipation profiles is plotted for all Seagliders that entered the FBC region. In this case only the average with respect to the 3° isotherm is computed and the vertical limits are reduced because some gliders did not encounter thick overflow layers. Some of these gliders spent only a few dives in the plume and are not as well suited for comparison with the VMP survey as sg005 (in the sense of not sufficiently sampling the mesoscale variability); however, the profile is displayed to show that the LEM is applicable to other Seagliders. We conclude that the Seaglider LEM accurately measures dissipation of TKE in the FBC to within a factor of 2.

Outside the FBC, on the less energetic IFR, microstructure measurements are not available for comparison with the Seaglider; therefore, we cannot rule out the possibility that the error is larger than the factor of 2 found in the channel. In order for the large eddy scaling [Eqs. (5) and (6)] to hold, the assumptions of a cascade

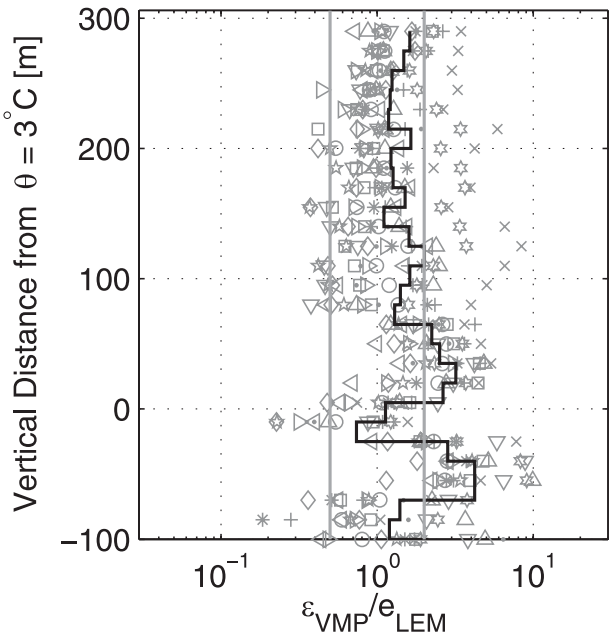

FIG. 7. Ratio of Seaglider LEM survey-averaged profiles to the VMP average profile for all 13 gliders in the FBC region. Each gray symbol represents a different Seaglider deployment. Averages are made with respect to distance from the 3°C isotherm. Black line shows the mean of all profiles; light gray lines show factor of 2 bounds on the estimate ratio. Glider deployments are represented by the following symbols: sg012 Sep 2007 (plus), sg104 Sep 2007 (open circle), sg014 Sep 2008 (asterisk), sg005 Sep 2009 (filled circle), sg103 Feb 2009 (multiplication symbol), sg101 Jun 2007 (open square), sg005 Jun 2008 (open diamond), sg016 Jun 2008 (open triangle), sg016 Jun 2009 (open upside-down triangle), sg016 Nov 2007 (open left-pointing triangle), sg102 Nov 2007 (open right-pointing triangle), sg103 Nov 2007 (filled star), and sg101 Nov 2008 (six-pointed star).

of energy through fully developed turbulence must be valid. This is certainly the case in the FBC, but may not be entirely valid on the IFR, necessitating caution when interpreting results from the ridge. There are, however, examples of energy cascades observed in lower energy environments (Lueck et al. 1997) and indications that Eq. (5) holds in regions of low -average dissipation containing individual energetic events (Peters et al. 1995).

2) PROBABILITY DISTRIBUTION FUNCTIONS IN LAYERS

In a second method of comparison between the VMP and Seaglider, dissipation estimates from the FBC region have been sorted into three layers: Atlantic (AL), interfacial (IL), and overflow layer (OL). The OL is the quasi-homogeneous layer of the bottom-attached overflow plume, defined as the cold (<3°C) layer above the bottom where the temperature gradient is less than 0.004°C m^{-1}. The AL is the ambient warm water, excluding the upper 50 m influenced by surface forcing.

The base of the AL is identified as the deepest point where the temperature is greater than 7.7°C and the temperature gradient is less than 0.01°C m^{-1}. The IL is the strongly stratified layer between the top of the OL and the bottom of the AL, where the bulk of the entrainment occurs. Typical thicknesses of these three layers in the FBC are approximately 70 m, 100 m, and more than 600 m for the OL, IL, and AL respectively. The three layers have been chosen because they represent regions where mixing is driven by different mechanisms: turbulence due to internal wave breaking in the ambient (AL), shear instabilities and entrainment (IL), and shear and boundary layer processes (OL).

Probability distribution functions (PDFs) of the Seaglider (colored lines) and the VMP (gray patch) in each layer are plotted in Fig. 8. The column on the left shows the distributions of the VMP and sg005, on which the calibration of c_ε is based. The right column adds the distributions of all Seagliders that made dives in the FBC region over the full three years of field work. Colored circles and gray squares show the maximum likelihood estimate (mle) for each Seaglider and VMP layer distribution. Horizontal bars plotted over the VMP mle squares show ½ and 2 times the mle. The Seaglider LEM distributions cover the range of the VMP distributions fairly well, with the best agreement in the OL and the worst in the IL. The stratification-dependent noise level of the LEM results in fewer measurements of low dissipation, causing disagreement between the VMP and Seaglider PDFs at low magnitude in the IL and to a lesser extent in AL. The dissipation estimates in the FBC are nearly lognormally distributed. Agreement at high values is most important for lognormally distributed variables. Agreement is better for the high-magnitude tail of the layer PDFs than for the low side. As in Fig. 7, the right column of Fig. 8 indicates that the LEM is applicable to the other Seagliders deployed in the FBC.

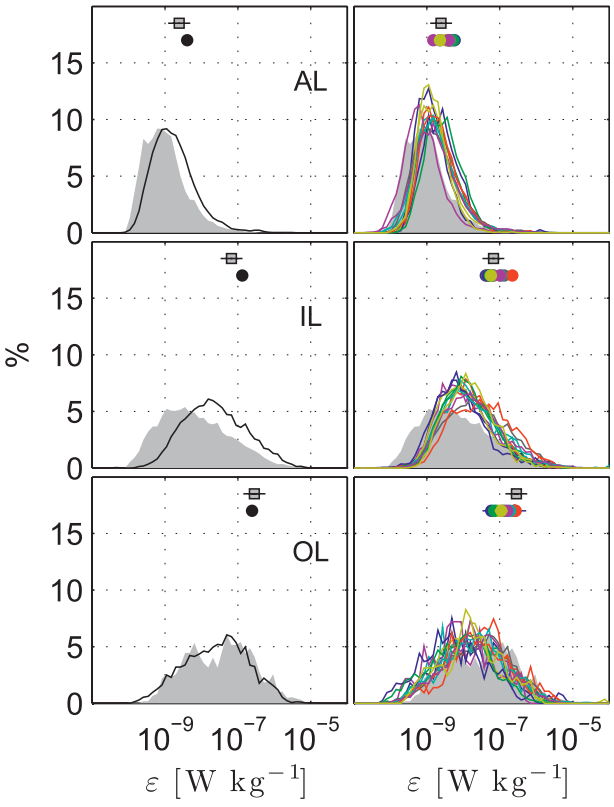

FIG. 8. PDFs of ε from the VMP (gray patch) and e from the Seaglider (colors) separated into the (top) Atlantic layer (AL), (middle) interfacial layer (IL), and (bottom) overflow layer (OL): (left) plot of the VMP and sg005 Jun 2008 deployment and (right) all Seagliders, from the three years of field work, that entered the FBC region along with the VMP. Colored dots plotted in each box show the maximum likelihood estimate (mle) of each distribution. The VMP mle is plotted just above the Seaglider values, with a horizontal line indication a factor of 2 range about the mle.

5. Results and discussion

a. Seaglider-inferred dissipation section

During its June 2008 deployment, sg005 spent a considerable amount of time targeting mooring B2, after which it traveled out of the FBC and completed a section normal to the IFR. Deployment-length sections of temperature and inferred dissipation rate plotted against profile number are presented in Fig. 9. Most of the first 400 profiles were in the FBC and constitute the subset used for comparison with the VMP. While trying to maintain its position near mooring B2, occasionally the glider was advected onto the Faroe Plateau (profiles 280–360) where strong anticyclonic flow was a persistent hazard to navigation. Those dives on the Faroe Plateau were not included in the intercalibration described in the preceding sections. Figure 9 shows high values of dissipation in the overflow plume (10^{-7} –10^{-6} W kg^{-1}), and much lower levels in the Atlantic layer above. Dissipation is elevated in the near surface layers throughout the deployment. Once the glider exited the FBC, around profile 400, dissipation decreased in the deep overflow layer. However, the Seaglider continued to observe slightly elevated dissipation above the ridge topography in a layer of diluted overflow water (profiles 450–600) and in the Iceland–Faroe Front (600–700). In the quiescent deep waters north of the IFR the sections show very little measurable dissipation.

The literature of the FBC overflow contains many claims that all of the important plume water mass

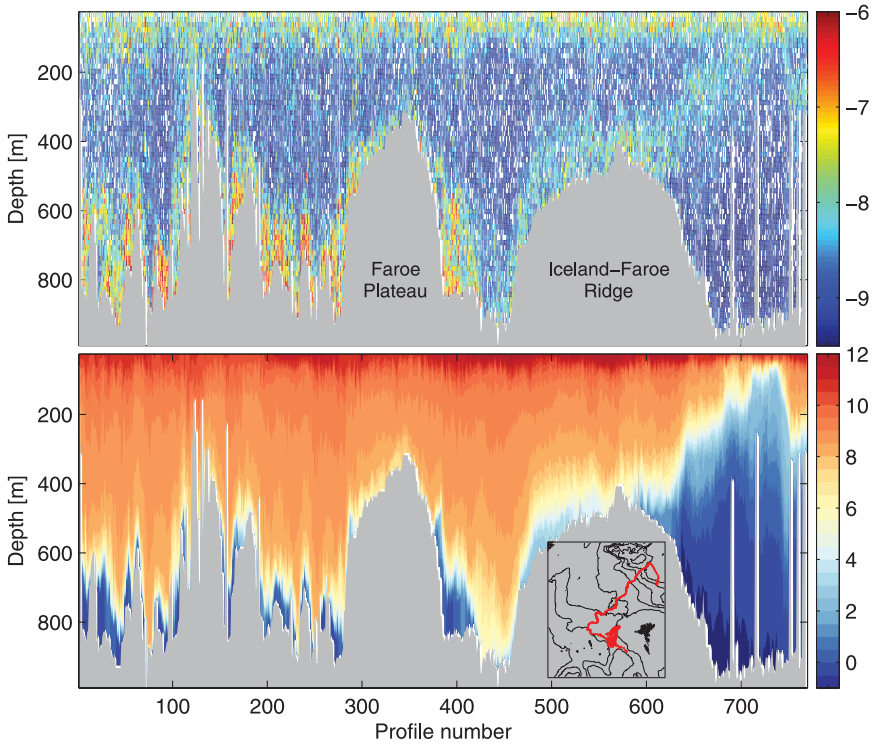

FIG. 9. (top) Depth vs profile number section of dissipation, $\log_{10}(e)$ [W kg^{-1}], from the entire sg005 deployment for which where each dive and climb is counted as a profile, and (bottom) corresponding temperature section (°C). Inset map shows the dive locations in red; the FBC dives may be seen in more detail in Fig. 2.

transformation happens immediately downstream of the FBC. It is clear from Fig. 9 (and Fig. 11, later) that the FBC terminus is an extremely active turbulent region. However, Fig. 9 also indicates that turbulence is elevated in the more diluted overflow layer on the IFR (profiles 450–600), which suggests that entrainment is still taking place downstream of the FBC.

b. *Mixing "hot spots"*

As mentioned above, previous studies have, justifiably, focused on the Faroe Bank Channel outflow where direct mixing estimates are now available on discrete ship tracks (Fer et al. 2010). An application of the LEM to the three years of Seaglider data allows us to describe the spatial distribution of mixing of the overflows along the IFR. Individual profiles of dissipation have been integrated over the thickness of the plume (50 m above the depth of the 27.65 isopycnal, H_p, to the bottom, HAB = 0) to produce the map of plume-integrated dissipation ($\rho_0 \int_0^{H_p} \varepsilon \, dz$) shown in Fig. 10. The integrals are multiplied by a reference density, $\rho_0 = 1027.4$ kg m^{-3}, to give units of watts per square meter. The field of plume-integrated dissipation reveals several interesting regions of enhanced mixing on the IFR, including the regions downstream of the primary and secondary sills of the FBC, and in a relatively undiluted IFR overflow plume adjacent to the Iceland shelf.

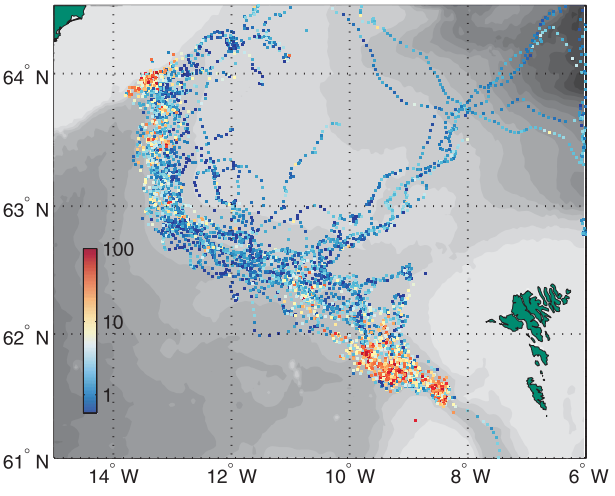

FIG. 10. Vertically integrated dissipation rates over the plume thickness, $\rho_0 \int_0^{H_p} \varepsilon \, dz$ (mW m^{-2}), from all Seaglider data.

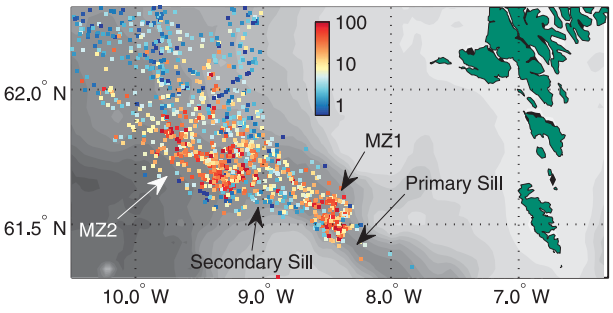

FIG. 11. Vertically integrated dissipation rates over the plume thickness, $\rho_0 \int_0^{H_p} \varepsilon \, dz$ (mW m^{-2}), in the FBC. MZ1 and MZ2 indicate the general region of the two enhanced mixing locations described in the text.

1) DOWNSTREAM OF PRIMARY AND SECONDARY FBC SILLS

The FBC region stands out as an energetic area where plume-integrated dissipation reaches a maximum of 330 mW m^{-2}, two orders of magnitude above most of the IFR. The Faroe Bank Channel contains both a primary and secondary sill separated by a shallow basin approximately 50 km long and 900 m deep. The primary sill, which is the narrowest and shallowest part of the channel, is 840 m deep and coincides with a horizontal constriction to about 10 km. The secondary sill, marking the terminus of the FBC, is wider and slightly deeper at ~850 m. Beyond the secondary sill the channel opens onto the Atlantic flank of the IFR. Downstream of both the primary and secondary sills plume-integrated dissipation jumps significantly in two distinct energetic regions (Fig. 11).

The energetic region downstream of the secondary sill corresponds well to the regions of enhanced mixing identified in discrete sections by Mauritzen et al. (2005) (100 km downstream of primary sill), Girton et al. (2006) (20–90 km) and Fer et al. (2010) (~80 km). The largest overflow velocities are often found in this region, where Fer et al. (2010) observed a maximum speed of 135 cm s^{-1}. Analysis of the Seaglider dataset (N. L. Beaird et al. 2012, unpublished manuscript) shows that downstream of the secondary sill the FBC overflow plume widens and thins considerably, while doubling its decent rate. This transition occurs as the plume evolves from a channelized gravity current to a dense flow on a slope. Numerical models produce plume widening in this region (Riemenschneider and Legg 2007; Seim et al. 2010), which is interpreted by Pratt et al. (2007) as a transverse hydraulic jump. Observations also suggest hydraulic control downstream of the secondary sill region (Girton et al. 2006) where Froude numbers become critical (Mauritzen et al. 2005; Fer et al. 2010; Seim et al. 2010). Additionally, these previous studies, as well as the Seaglider data, indicate that the FBC plume bifurcates into a shallow and a deep branch at a topographic bump located at 61.9°N, 10.12°W.

All of these observations are consistent with the large region of enhanced turbulent dissipation centered around 61.75°N, 9.5°W shown in Fig. 11, referred to as "Mixing Zone 2" (MZ2). Plume-integrated dissipation is elevated (up to 330 mW m^{-2}) from west of the secondary sill at about 9°W to the topographic feature at 10.12°W. The mean plume-integrated dissipation over the whole area is 19 mW m^{-2}. The Seaglider is depth-limited to 1000 m, so from Fig. 11 it is unclear how far downstream the high dissipation extends in the deep branch of the overflow. However, the extent of the elevated dissipation region can be seen on the shallow side of the plume. It appears that the highest dissipation in the shallow branch has relaxed to IFR mean values by 100 km downstream of the primary sill (~62°N, 9.5°W).

The high spatial resolution of the Seaglider surveys resolves two different zones of enhanced mixing: the previously discussed region beyond the secondary sill (MZ2) and a region immediately downstream from the primary sill (Mixing Zone 1, or MZ1) (Fig. 11). Coarser section spacing in previous studies of the FBC has not resolved the separation between these two regions. MZ1 and a relatively quiescent region separating it from MZ2 are contained in the basin between the sills. MZ1 has a maximum plume-integrated dissipation of 195 mW m^{-2}, and the mean is 21 mW m^{-2}, slightly higher than in MZ2. Girton et al. (2006) use three different methods to locate the section of hydraulic control in the FBC, finding general agreement that the critical section lies between 20 and 90 km downstream of the primary sill. The most confident estimate was found to be 50 km downstream at the secondary sill. That there are two distinct regions of enhanced dissipation in Fig. 11 seems consistent with the spread in the estimates of the location of hydraulic control, perhaps suggesting time variability of the control section location.

2) WESTERN VALLEY JET

A previously undocumented area of enhanced turbulent dissipation is located adjacent to the Iceland shelf at the northwestern end of the IFR (Fig. 10). A slight depression in the ridge crest where the IFR intersects the Iceland shelf, sometimes referred to as the Western Valley (WV), has long been thought to provide a pathway for a portion of the dense overflow across the IFR. Current meter records in the region indicate long-term near bottom velocities are steady and directed along the Iceland shelf with mean speeds of 50 cm s^{-1} (Perkins et al. 1998). It is unclear from the Perkins et al. study if

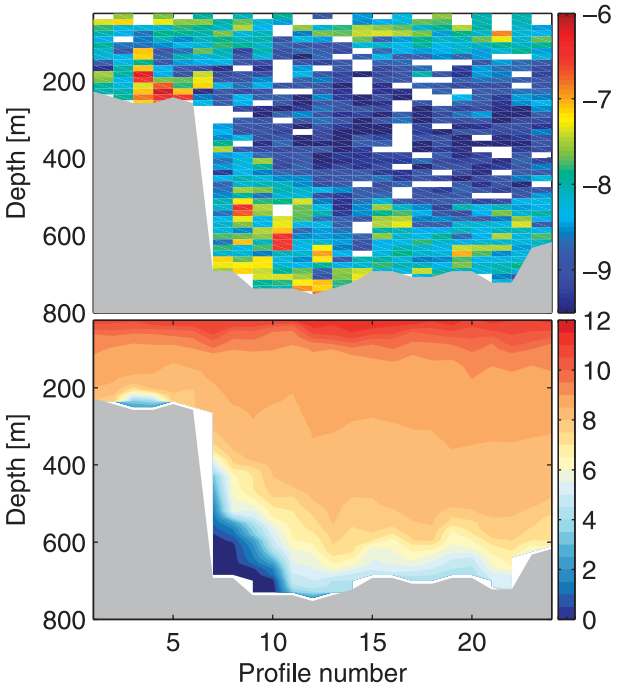

FIG. 12. (top) Section of dissipation, $\log(\epsilon)$ (W kg^{-1}), from sg016 crossing the Western Valley 24–25 July 2008. Depth vs profile number where each dive and climb is counted as a profile. (bottom) Corresponding temperature section (°C).

the steady near bottom velocities imply a steady overflow transport because contemporaneous temperature records are not published with the current meter data. Many (31) Seaglider transects where made in the region, often observing the WV overflow in a 10 km wide jet with 50–70 cm s^{-1} absolute geostrophic velocities. Figure 12 shows one such crossing of the WV overflow jet by sg016 in late July 2008. The maximum absolute geostrophic velocity in the overflow during that crossing was 57 cm s^{-1}. The temperature section shows the narrow jet of cold water balanced against the Iceland shelf break. The accompanying dissipation section reveals elevated turbulence in the jet. The set of Seaglider transects intersecting the Iceland shelf indicates that the overflow transport in the WV is much more variable than the current meter records of Perkins et al. would suggest. Observed dense water ($\sigma_\theta \geq 27.8$ kg m^{-3}) overflow transports calculated from absolute geostrophic velocities range between 0.07 and 2.13 Sv in six transects made over a 12 day period in June/July 2009 (N. L. Beaird et al. 2012, unpublished manuscript). An episodic overflow event of similar duration appears in the observations of Perkins et al. (1994).

Figure 13 shows that the narrow WV overflow region, delineated by the low bottom temperatures in the right panel, is also a region of high dissipation. Maximum plume-integrated dissipation reaches 250 mW m^{-2}, with a mean value 13 mW m^{-2} in the WV overflow jet. A clear advantage of the Seaglider LEM is the identification of regions such as this one, which was observed during the course of a survey designed to map the hydrography of overflows on the IFR. Dedicated microstructure surveys in the region have never been carried out, so it is only through this ancillary inferred Seaglider measurement that the energetic region was discovered. While the Atlantic water above the overflow in the WV is much the same as that overlying the FBC, there are gradients in Atlantic water properties across the ridge. Additionally, very fresh coastal water from Iceland is occasionally advected off the shelf into the surface waters of the WV. Mixing between the overflow waters and different ambient waters influences the downstream properties of the overflow (Price and Baringer 1994), potentially resulting in distinct contributions to North Atlantic Deep Water from the WV and FBC overflows. Therefore, mapping the regions of energetic turbulence and the ambient properties by Seagliders provides insight into dense water production by these overflows.

6. Summary

Levels of turbulent dissipation have been mapped in one of the two major source regions of North Atlantic Deep Water. Mixing and entrainment in these small overflow regions are of great importance to the global abyssal circulation and the climate system. A scaling has been investigated that infers dissipation of turbulent kinetic energy from finescale vertical velocity observed by an autonomous vehicle.

The large-eddy method (LEM) defined here assumes that most of the kinetic energy in a turbulent eddy is dissipated in the time it takes to overturn once. The scaling requires a length scale and a velocity scale of these eddies. The length scale is taken to be the Ozmidov length scale, which is the largest size of an overturn in stratified flow. The velocity scale is estimated from the vertical velocity fluctuations, after removing the low wavenumber and internal-wave-induced contribution by a suitably chosen high-pass filter, as the root-mean-square over several eddy lengths. The dissipation estimate depends on a proportionality constant, which is determined by calibrating the results from a dedicated Seaglider, collocated with a cruise, against dissipation measurements from a shipboard microstructure survey. A comparison between the Seaglider-inferred dissipation and the microstructure measurements indicate that the LEM reproduces the direct measurements within a factor of 2. Survey-averaged profiles of dissipation rate covary over several orders of magnitude. The noise level

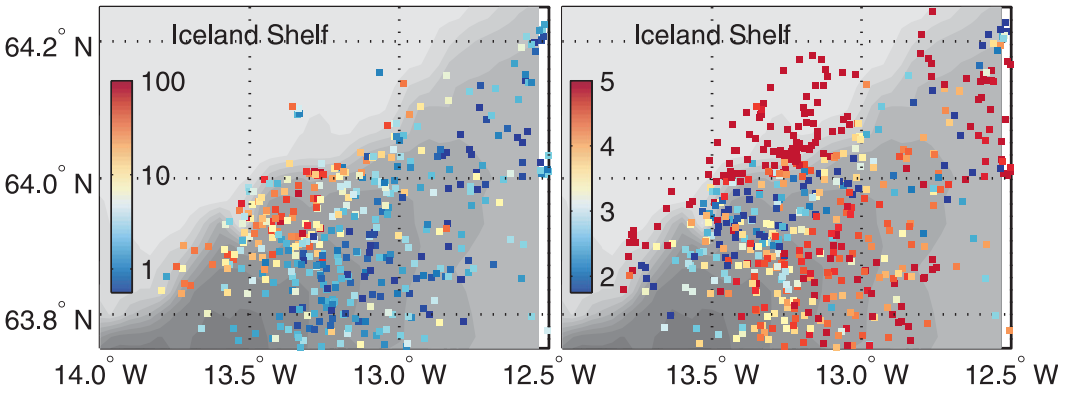

FIG. 13. (left) Vertically integrated dissipation rates over the plume thickness, $\rho_0 \int_0^{H_p} \varepsilon \, dz$ (mW m^{-2}), for the Iceland shelf break overflow and (right) bottom temperature (°C) near the Iceland shelf break.

of the LEM is dependent on stratification and varies between 2.5×10^{-9} and 1×10^{-8} W kg^{-1} in the Faroe Bank Channel. The LEM was then tested on 12 other Seagliders that entered the FBC region over three years between November 2006 and November 2009, using the portions of the data collected in the vicinity of the cruise site. The survey-averaged profiles from each glider agreed well with the microstructure measurements.

The LEM, once calibrated, was then applied to the entire dataset of the 13 Seagliders deployed on the Iceland–Faroe Ridge. Maps of plume-integrated dissipation revealed three regions of enhanced mixing. The largest dissipation rates were found in a mixing zone (MZ2) downstream of the secondary FBC sill, consistent with previously documented observations. MZ2 corresponds to suspected regions of hydraulic control, the bifurcation of the overflow plume, as well as a significant widening, thinning, and increase in descent rate. The Seaglider data defined the size and diffuse location of MZ2 in a way previously unrealized by discrete ship tracks. Another FBC high energy region was found in MZ1 just downstream of the primary FBC sill. This region is separated from MZ2 by a relatively quiet region at the western end of the shallow basin between the two sills. Previous ship-based observations did not resolve these two distinct regions, which likely led to the range of values given for the downstream locations of the highest FBC mixing.

Finally a third, previously unknown, region of enhanced dissipation was found in a narrow jet of IFR overflow water leaning against the Iceland shelf break. The values of plume-integrated dissipation in this Western Valley jet were nearly as large as in the FBC. The location of energetic turbulence, and presumably vertical mixing, in the WV is important as the properties of the entrained water mass influence the eventual IFR contribution to North Atlantic Deep Water.

A method has been defined from which an estimate of dissipation of TKE can be made from a standard Seaglider. Comparison with a microstructure survey indicates that the Seaglider large-eddy method is valid within a factor of 2 in the energetic FBC. The LEM does not have the high accuracy of more direct microstructure measurements but it offers a relatively economical additional measurement from the increasingly common glider surveys worldwide. In particular the advantage of the LEM is in mapping regions of energetic turbulence with high spatial and temporal resolution. Used as an exploratory vehicle, the Seaglider and LEM may be able to provide a focus for more detailed process studies.

Acknowledgments. The Seaglider measurements described here were collected under National Science Foundation Grant OCE0550584. The Shipboard and mooring measurements were made under Project 204867 funded by the Research Council of Norway. The measurements would not have been possible without the help of Bill Fredericks, Kirk O'Donnell, the Faroe Marine Research Institute, and the crews of the R/S *Magnus Heinason* and R/V *Håkon Mosby*. The first author would like to thank Eric D'Asaro and Eleanor Frajka-Williams for many enlightening conversations regarding vertical velocities and turbulence.

REFERENCES

Darelius, E., I. Fer, and D. Quadfasel, 2011: Faroe Bank Channel overflow: Mesoscale variability. *J. Phys. Oceanogr.,* **41,** 2137–2154.

D'Asaro, E. A., and R. C. Lien, 2000a: Lagrangian measurements of waves and turbulence in stratified flows. *J. Phys. Oceanogr.,* **30,** 641–655.

——, and ——, 2000b: The wave–turbulence transition for stratified flows. *J. Phys. Oceanogr.,* **30,** 1669–1678.

Dewey, R., 1999: Mooring design and dynamics—A Matlab package for designing and analyzing oceanographic moorings. *Mar. Models,* **1,** 103–157.

Dillon, T. M., 1982: Vertical overturns: A comparison of Thorpe and Ozmidov length scales. *J. Geophys. Res.,* **87,** 9601–9613.

Duncan, L. M., H. L. Bryden, and S. A. Cunningham, 2003: Friction and mixing in the Faroe Bank Channel outflow. *Oceanol. Acta,* **26,** 473–486.

Eriksen, C. C., T. J. Osse, R. D. Light, T. Wen, T. W. Lehman, P. L. Sabin, J. W. Ballard, and A. M. Chiodi, 2001: Seaglider: A long-range autonomous underwater vehicle for oceanographic research. *IEEE J. Oceanic Eng.,* **26,** 424–436.

Fer, I., G. Voet, K. S. Seim, B. Rudels, and K. Latarius, 2010: Intense mixing of the Faroe Bank Channel overflow. *Geophys. Res. Lett.,* **37,** L02604, doi:10.1029/2009GL041924.

Frajka-Williams, E., C. Eriksen, P. Rhines, and R. Harcourt, 2011: Determining vertical water velocities from Seaglider. *J. Atmos. Oceanic Technol.,* **28,** 1641–1656.

Gargett, A., 1999: Velcro measurement of turbulent kinetic energy dissipation rate ε. *J. Atmos. Oceanic Technol.,* **16,** 1973–1993.

Geyer, F., S. Østerhus, B. Hansen, and D. Quadfasel, 2006: Observations of highly regular oscillations in the overflow plume downstream of the Faroe Bank Channel. *J. Geophys. Res.,* **111,** C12020, doi:10.1029/2006JC003693.

Girton, J. B., L. J. Pratt, D. A. Sutherland, and J. F. Price, 2006: Is the Faroe Bank Channel overflow hydraulically controlled? *J. Phys. Oceanogr.,* **36,** 2340–2349.

Hansen, B., and S. Østerhus, 2000: North Atlantic–Nordic Seas exchanges. *Prog. Oceanogr.,* **45,** 109–208.

——, and ——, 2007: Faroe Bank Channel overflow 1995–2005. *Prog. Oceanogr.,* **75,** 817–856.

Hubbard, R. M., 1980: Hydrodynamics technology for an Advanced Expendable Mobil Target (AEMT). APL-UW Tech. Rep. 8013, 34 pp.

Kida, S., J. Price, and J. Yang, 2008: The upper-oceanic response to overflows: A mechanism for the Azores Current. *J. Phys. Oceanogr.,* **38,** 880–895.

Kolmogoroff, A., 1941: The local structure of turbulence in incompressible viscous fluid for very large Reynolds numbers. *Dokl. Akad. Nauk SSSR,* **30,** 299–303.

Legg, S., and Coauthors, 2009: Improving oceanic overflow representation in climate models: The gravity current entrainment climate process team. *Bull. Amer. Meteor. Soc.,* **90,** 657–670.

Lueck, R. G., D. Huang, D. Newman, and J. Box, 1997: Turbulence measurement with a moored instrument. *J. Atmos. Oceanic Technol.,* **14,** 143–161.

Mauritzen, C., J. Price, T. Sanford, and D. Torres, 2005: Circulation and mixing in the Faroese Channels. *Deep-Sea Res.,* **52,** 883–913.

Merckelbach, L., D. Smeed, and G. Griffiths, 2010: Vertical water velocities from underwater gliders. *J. Atmos. Oceanic Technol.,* **27,** 547–563.

Moum, J. N., 1996: Energy-containing scales of turbulence in the ocean thermocline. *J. Geophys. Res.,* **101,** 14 095–14 109.

Perkins, H., T. S. Hopkins, S. A. Malmberg, P. M. Poulain, and A. Warn-Varnas, 1998: Oceanographic conditions east of Iceland. *J. Geophys. Res.,* **103,** 21 531–21 542.

——, T. J. Sherwin, and T. Hopkins, 1994: Amplification of tidal currents by overflow on the Iceland–Faroe Ridge. *J. Phys. Oceanogr.,* **24,** 721–735.

Peters, H., M. C. Gregg, and T. B. Sanford, 1995: Detail and scaling of turbulent overturns in the Pacific Equatorial Undercurrent. *J. Geophys. Res.,* **100,** 18 349–18 368.

Pratt, L. J., U. Riemenschneider, and K. R. Helfrich, 2007: A transverse hydraulic jump in a model of the Faroe Bank Channel outflow. *Ocean Modell.,* **19,** 1–9.

Price, J. F., and M. O. Baringer, 1994: Overflows and deep water production by marginal seas. *Prog. Oceanogr.,* **33,** 161–200.

Riemenschneider, U., and S. Legg, 2007: Regional simulations of the Faroe Bank Channel overflow in a level model. *Ocean Modell.,* **17,** 93–122.

Saunders, P. M., 1990: Cold outflow from the Faroe Bank Channel. *J. Phys. Oceanogr.,* **20,** 29–43.

Seim, K. S., and I. Fer, 2011: Mixing in the stratified interface of the Faroe Bank Channel overflow: The role of transverse circulation and internal waves. *J. Geophys. Res.,* **116,** C07022, doi:10.1029/2010JC006805.

——, ——, and J. Berntsen, 2010: Regional simulations of the Faroe Bank Channel overflow using a σ-coordinate ocean model. *Ocean Modell.,* **35,** 31–44.

Smyth, W., and S. A. Thorpe, 2012: Glider measurements of overturning in a Kelvin–Helmholtz billow train. *J. Mar. Res.,* **70,** 119–140.

Taylor, G. I., 1935: Statistical theory of turbulence. *Proc. Roy. Soc. London,* **A151,** 421–454.

Tennekes, H., and J. L. Lumley, 1972: *A First Course in Turbulence*. The MIT Press, 300 pp.

Thorpe, S. A., 2005: *The Turbulent Ocean*. Cambridge University Press, 439 pp.